Piezo-promoted regeneration of Fe^{2+} boosts peroxydisulfate activation by $Bi_2Fe_4O_9$ nanosheets

Chuangjian Su [a], Ruhong Li [b], Chaolin Li [a,c,*], Wenhui Wang [a,**]

[a] School of Civil and Environmental Engineering, Harbin Institute of Technology, Shenzhen, Shenzhen 518055, China
[b] School of Materials Science and Engineering, Zhejiang University, Hangzhou 310027, China
[c] State Key Laboratory of Urban Water Resource and Environment, School of Environment, Harbin Institute of Technology, Harbin 150090, China

ARTICLE INFO

ABSTRACT

The application of promising persulfate-based advanced oxidation processes (AOPs) for environment remediation is limited by the poor charge separation and the sluggish kinetic for active centers regeneration of the catalysts. Piezocatalytic activation has been proposed to solve the above concern recently, but little is known on its mechanism. Herein, novel piezocatalyst $Bi_2Fe_4O_9$ nanosheets (BFO NSs) are demonstrated to significantly improve peroxydisulfate (PDS) activation efficiency via piezocatalysis, resulting $SO_4^{\bullet-}$ and $\bullet OH$ as the dominant active species for organic pollutants degradation. Further DFT calculations and experimental investigations confirm that the Fe^{2+} in BFO NSs as active sites donate electrons for PDS to generate $SO_4^{\bullet-}$, and simultaneously that the piezo-electrons can accelerate the regeneration of Fe^{2+}, thus leading to the superior catalytic activity. This work provides atomic-scale insights of catalytic sites and mechanisms of piezocatalytic PDS activation and may inspire the development of more efficient piezocatalysts and AOPs.

1. Introduction

Advanced oxidation process (AOPs) based on persulfates (PS) has attracted increasing attentions in environmental remediation due to the strong oxidizing capability and longer half-life periods of $SO_4^{\bullet-}$ (30–40 μs for $SO_4^{\bullet-}$ vs. 10^{-3} μs for $\bullet OH$) [1–3]. Intensive effort has been devoted to finding efficient catalysts for PS activation over the past decade [4–6]. Unfortunately, most of them are suffer from low catalytic activity mainly due to the limited charge separation and the sluggish kinetic for regeneration of the catalytic center [7,8]. Thus, it is imperative to accelerate the regeneration of catalytic center (e.g., Fe^{2+}) for enhanced catalytic activity of PS activation.

Piezocatalysis is another promising technique for environmental remediation, where piezo-charges, which is generated through catalyst deformation rooted from vibrational energy (e.g., water flowing and ultrasound, etc.) [9–11], can capture water/oxygen to generate redox oxidation species for organic pollutants removal [12–15]. To take the advantage of piezo-electrons for activating PS, piezocatalytic PS activation over traditional piezocatalysts (e.g., $BaTiO_3$) has been proposed and proved to be a promising approach for wastewater purification [16]. For example, Peng et al. disclosed that $BaTiO_3$ nanowires exhibited superior piezocatalytic activity for peroxydisulfate activation than $BaTiO_3$ nanoparticles [17]. Xia et al. successfully developed Ag modified $BaTiO_3$ as an efficient piezoelectric catalyst for Escherichia coli inactivation via PS activation [18]. However, $BaTiO_3$ is toxic and its performance for traditional PS activation is poor [19]. It is worth mentioning that Fe-based materials are reported as the most promising catalysts candidates for tranditional PS activation due to their environmental friendliness and low cost [20,21], although the further improvement of catalytic activity is limited by the regeneration of Fe^{2+} active centers. On the other hand, little is known on the active sites and catalytic mechanisms of piezocatalysts in the piezocatalytic PS activation, as well as the role of piezo-electrons in catalytic PS activation, which is not conducive to the development of efficient piezocatalysts for activating PS.

Herein, we successfully synthesized novel $Bi_2Fe_4O_9$ nanosheets (BFO NSs) as a piezocatalyst for activating persulfate and unveil the above mechanism. The piezocatalytic peroxydisulfate (PDS) activation with BFO NSs can efficiently degrade Bisphenol A in wider pH range (2.5–9.2). The major active species in piezocatalytic PDS activation process over BFO NSs were confirmed to $SO_4^{\bullet-}$ and $\bullet OH$. Furthermore, it is disclosed that Fe^{2+} as active centers activate the PDS into $SO_4^{\bullet-}$ through donating electrons, and the piezo-electrons facilitate the

regeneration of Fe^{2+}, thus ensuring the high catalytic performance of piezocatalytic PDS activation.

2. Materials and methods

2.1. Chemicals

All reagents were analytical grade and used as received. Bismuth nitrate ($Bi(NO_3)_3 \bullet 5H_2O$), iron chloride hexahydrate ($FeCl_3 \bullet 6H_2O$), sodium hydroxide (NaOH), ethylene glycol, bisphenol A (BPA), ibuprofen (IBP), sulfamethoxazole (SMX), carbamazepine (CBZ), atrazine (ATZ), peroxydisulfate ($Na_2S_2O_8$, PDS), sodium bicarbonate ($NaHCO_3$), sodium nitrate ($NaNO_3$), sodium chloride (NaCl), calcium chloride ($CaCl_2$), magnesium chloride ($MgCl_2$), humic acid (HA), p-Benzoquinone (p-BQ), methanol (CH_3OH, MeOH), ethanol (C_2H_6O, EtOH), phenol (C_6H_5OH, PhOH), sodium azide (NaN_3), furfuryl alcohol (FFA), hydroxylammonium chloride ($H_3NO \cdot HCl$), potassium iodide (KI), 1,10-Phenanthroline Monohydrate ($C_{12}H_8N_2 \cdot H_2O$), 2,2,6,6-tetramethyl-4-piperidino (TEMP), 5,5-dimethyl-1-pyrroline N-oxide (DMPO) were purchased from Aladdin Chemistry Co., Ltd, China. The deionized water was used throughout the experiments.

2.2. Catalyst preparation

The BFO NSs was synthesized by the slightly modified hydrothermal method referred to previous report [22]. Firstly, the $Bi(NO_3) \cdot 5H_2O$ and $FeCl_3 \cdot 6H_2O$ with a 0.85:1 molar ratio were dissolved in ethylene glycol solution under mechanical stirring. Next, 200 mL deionized water was added and the pH was adjusted to 11 by dropping concentrated ammonia. The obtained brown precipitates were washed with deionized water, added to NaOH solution (14 mol·L^{-1}) to form suspension, which was sealed into a 50 mL stainless steel autoclave for hydrothermal treatment at 180 °C for 72 h. The obtained sample was washed by deionized water and ethanol followed by drying at 60 °C.

2.3. Catalyst characterization

The crystal structure of the catalyst was characterized via X-ray powder diffractometer (XRD, Dandong Haoyuan DX-27) system with Cu Ka radiation (40 kV and 25 mA). The catalyst morphology and surface element analyses were obtained by a scanning electron microscope (SEM, FEI Talos S-FEG) with energy dispersive X-ray spectroscopy (EDS) detector unit. Transmission electron microscope (TEM) image, lattice fringes and selected-area electron diffraction (SAED) pattern were acquired using a transmission electron microscopy (TEM, FEI Tecnai Spirit). The Brunauer−Emmett−Teller (BET) specific surface area of BFO NSs was acquired by N_2 adsorption and desorption isotherm (ADI) on a surface area and porosimetry analyzer (ASAP2460). The valence states of elements in catalyst were investigated by X-ray photoelectron spectroscopy (XPS, Thermo Scientific Nexsa) and all XPS spectra were calibrated using the binding energy of C1s peak at 284.8 eV. The UV–vis diffuse reflectance spectra (DRS) measurement was carried out using an UV–vis spectrophotometer (Shimadzu UV-3600) equipped with an integrating sphere. The Piezoresponse Force Microscopy (PFM) measurement was performed on an atomic force microscope (AFM, Dimension Icon Bruker).

2.4. Catalytic activity and analysis methods

The BPA degradation was selected to evaluate piezocatalytic activity of BFO NSs for PDS activation. Firstly, 10 mL mixture solution of BPA (5 mg/L) and BFO NSs (1.5 g/L) was stirred at the low stirring speed of 80 rpm for 60 min to achieve the equilibrium of the adsorption-desorption. After that, the stirring speed was increased to 1400 rpm and the PDS was added to trigger the piezocatalytic PDS activation process [9,23]. At every 5 min, 0.2 mL aqueous solution was withdrawn and added to 1.8

mL ethanol solution (2000 mM) to terminate reaction, and then the mix solution filtered through a 0.22 μm filter membrane. The concentration of BPA was analyzed by a liquid chromatography (H-class Plus, Waters, USA) using a C18 column. The mobile phase was consisted of acetonitrile and water (50:50 v/v) and the detection wavelength is set to 224 nm [24]. The intermediates generated in BPA degradation process were identified via a Gas Chromatography-Mass Spectrometer (GC-MS, Agilent, 7590B-5977B). The initial pH values were adjusted using HCl or NaOH. The dissolved Fe and Bi concentrations were obtained by inductively coupled plasma optical emission spectrometer (ICP–OES, PerkinElmer, Optima 8000). The Mott-Schottky curve and piezo-current density were measured using an electrochemical workstation (Corrtest CS350H) using a Pt wire and Ag/AgCl electrode as counter electrode and reference electrode, and 0.2 M Na_2SO_4 aqueous solution was used as the electrolyte. The reactive species were determined by an electron paramagnetic resonance (EPR) spectrometer (Bruker A300).

### 2.5. Theoretical calculation studies

The ab initio molecular dynamics (AIMD) simulations were performed using the freely available CP2K/Quickstep package [25]. The Density Functional Theory (DFT) implemented in CP2K is based on a hybrid Gaussian plane wave scheme. The molecular orbitals of the valence electrons are expanded into DZVP-MOLOPT-Goedecker−Teter−Hutter (GTH) basis sets, whereas the interaction with the cores is described through GTH pseudopotentials. The efficient solution of the Poisson equation within the PBC is obtained in the reciprocal space by the expansion of the electronic density into a plane-wave basis set truncated at the energy cutoff of 400 Ry. We used the Perdew-Burke-Ernzerhof functional to describe exchange-correlation effects, and the dispersion correction was applied in all calculations with the Grimme D3 method. Because of the large size of the cells, only the Gamma point in the reciprocal space was used in our calculations. AIMD simulations were performed at 298.15 K using a Nose thermostat to allow fast equilibration. At least 10 ps of dynamic simulations was performed. The computations of the minimum energy paths and barriers were carried out with the climbing image elastic band (CI-NEB) method [26].

The bulk crystal structure was obtained from Materials Project Database (https://materialsproject.org/) with a crystal id of mp-504615. The $Bi_2Fe_4O_9$ (001) surface was modeled by a p(2 × 2) periodic supercell slab with 6 at. layers. The vacuum space between the slab and its periodic image is 15 Å, and the size of $Bi_2Fe_4O_9$ (001) supercell is $12.189 \times 16.160 \times 22.996$ Å^3. S_2O_8 molecule was placed on the cathode surface with removing two electrons from the system (referred to $S_2O_8^{2-}$). To describe correctly the energetics of the Fe 3d states, Hubbard correction with $U_{eff} = 5.30$ eV (J = 0.0 eV) was introduced in our calculations.

3. Results and discussion

3.1. Characterization of catalyst

The XRD pattern of as-synthesized catalyst (Fig. 1a and Fig. S1) can be indexed to $Bi_2Fe_4O_9$ with orthorhombic structure (JCPDS No. 25–0090). Apparently, the relative intensity of (001) diffraction peak of $Bi_2Fe_4O_9$ is stronger than other peaks, indicating the exposure of more {001} facets. The SEM images demonstrate that the thickness and edge length of $Bi_2Fe_4O_9$ are around 85 nm and 1.2 μm, respectively (Figs. 1b and S2). The nanosheet morphology of $Bi_2Fe_4O_9$ with uniform elemental distribution is further confirmed by its TEM image (insert of Fig. 1c) and Fig. 1d. HRTEM image (Fig. 1c) shows that the lattice fringe is 0.596 and 0.583 nm, consistent with the interplanar distance of the (001) and (110) planes of the orthorhombic $Bi_2Fe_4O_9$. Furthermore, the corresponding SAED pattern verifies the single crystalline nature of the BFO NSs (insert of Fig. 1c). The N_2 adsorption and desorption isotherm (ADI)
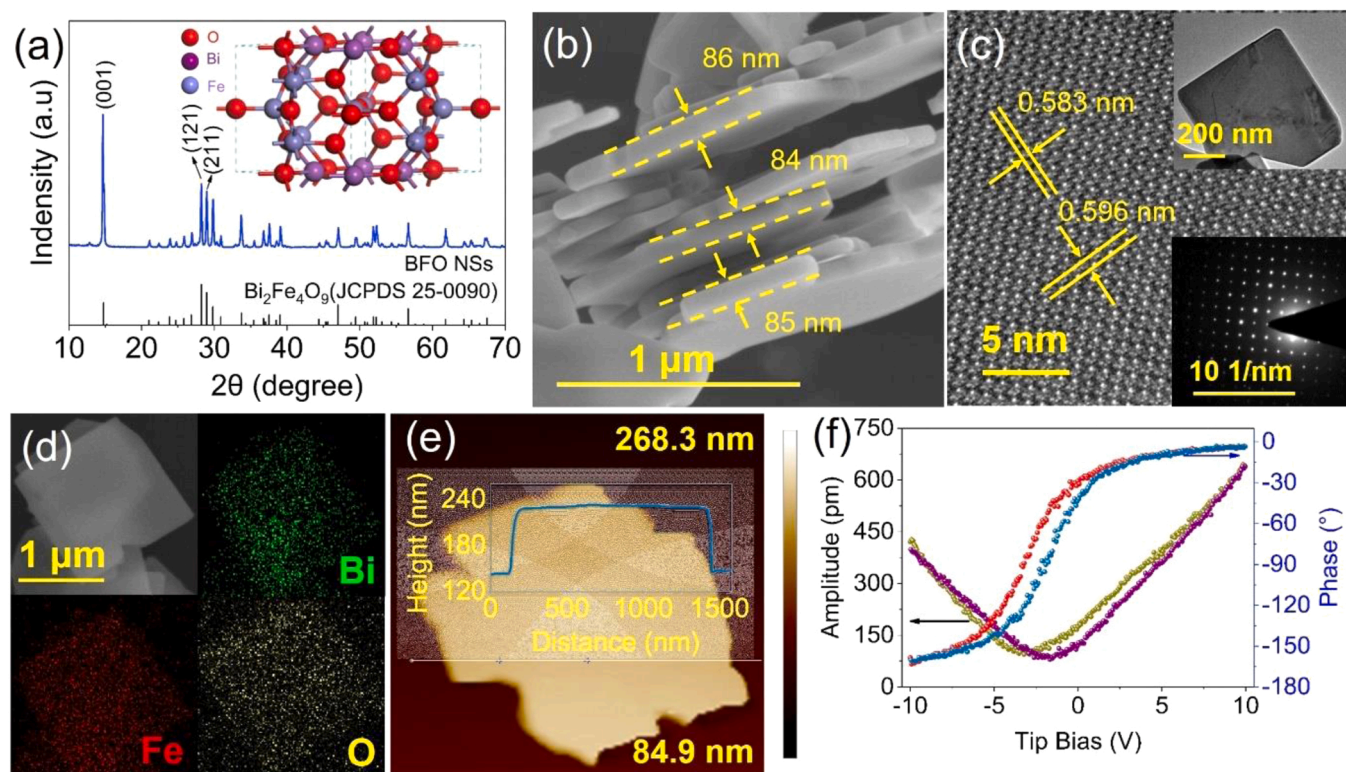
Fig. 1. (a) XRD pattern (the inset is crystal structure of BFO NSs), (b) SEM image, (c) HRTEM image (the inset is TEM image and SAED pattern, respectively), (d) element mapping, (e) AFM image (the inset is the corresponding height curve), (f) amplitude butterfly loops and phase hysteresis loops for BFO NSs.

for BFO NSs suggests there is slit-like mesopores in BFO NSs (Fig. S3) [27,28], and specific surface area is determined to be 3.5 $m^2 \ g^{-1}$. The piezoelectricity of the BFO NSs is verified by atomic force microscopy (AFM) with piezoresponse force microscopy (PFM) module. The AFM morphology and corresponding height curve well matches the SEM results (Figs. 1e and S4). The butterfly amplitude curve exhibits obvious variation in the amplitude and the phase angle in the local hysteresis loop changes by 160° (Fig. 1f), confirming the piezoelectricity of BFO NSs [23,29,30].
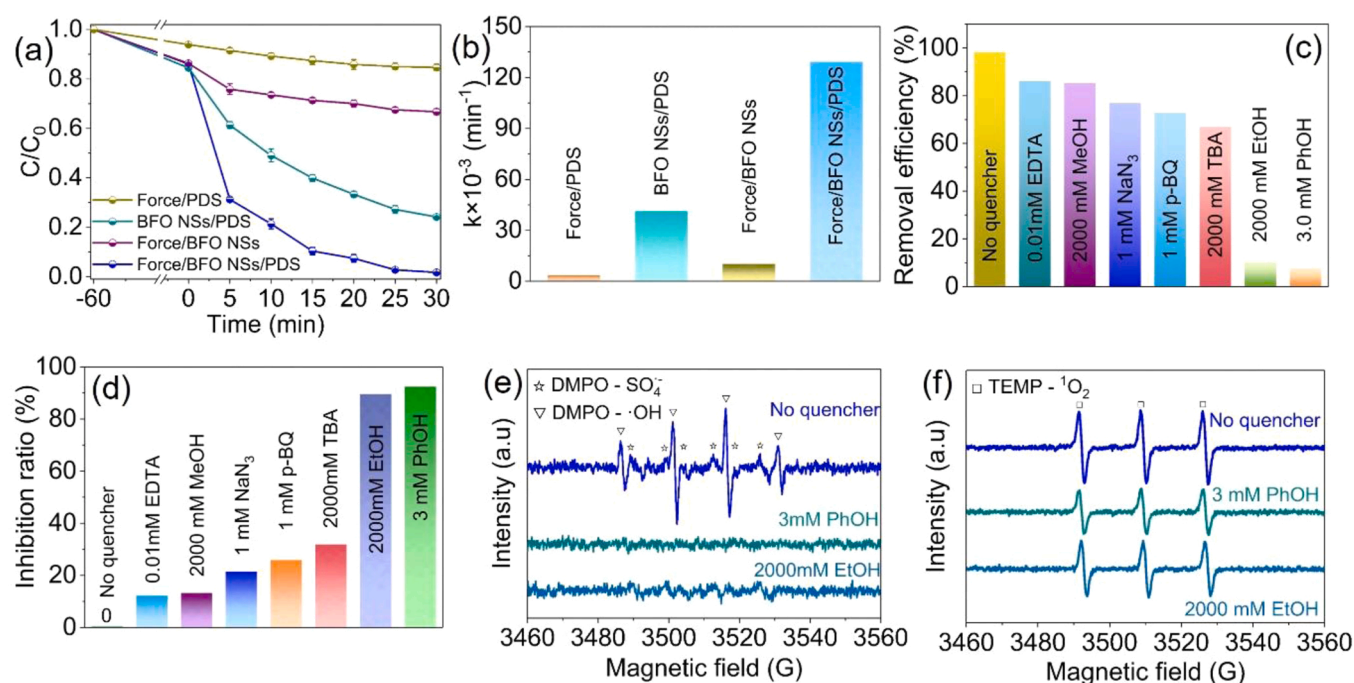
Fig. 2. (a) The BPA degradation curves and (b) corresponding kinetic rate constants in different systems. (c) Removal efficiency and (d) inhibition ratio of BPA degradation in the presence of different quenchers. (e) EPR spectra of generated $SO_4^{\bullet-}$ and •OH. (f) EPR spectra for $^1O_2$. Reaction conditions for (a-d): [catalyst] = 1.5 g/L, [PDS] = 1 mM, [BPA] = 5 mg/L, initial pH 6.8.

3.2. Catalytic activity and generated active species

The piezocatalytic efficiency of BFO NSs for PDS activation was evaluated by the degradation of BPA (Fig. 2a). The Force/PDS, BFO NSs/PDS and Force/BFO NSs systems remove 15.3%, 75.8% and 33.3% of BPA respectively, which clearly confirms that the BFO NSs could activate PDS and the applied force can induce BFO NSs to generate piezocharges for BPA degradation [31–33]. Notably, when the applied force was combined with BFO NSs/PDS process to construct Force/BFO NSs/PDS system (referred to piezocatalytic PDS activation system over BFO NSs), the removal efficiency of BPA within 30 min significantly increases to 98.3%, which is 22.5% higher than that of the BFO NSs/PDS system. It is found that the degradation of BPA followed the first-order reaction model (Fig. S5). The degradation rate constant (k value) for Force/BFO NSs/PDS system is around 3.1 times higher than that of BFO NSs/PDS system (Figs. 2b and S6). Moreover, it is also found that piezocatalytic activation over BFO NSs can accelerate the decomposition of PDS and increasing the stirring speed (i.e., applied force) can enhance the BPA degradation in Force/BFO NSs/PDS system (Fig. S7). These results indicate that the piezoelectricity of BFO NSs significantly enhanced the catalytic efficiency for PDS activation.

Remarkably, 97.9% of BPA was degraded in 10 min in the Force/BFO NSs /PDS system when BFO NSs, PDS and BPA concentrations are 2 g/L, 1 mM and 5 mg/L, respectively (Figs. S8 and S9). It worth mentioning that the Force/BFO NSs /PDS system maintains the high catalytic performance in the presence of common organic matter (i.e., HA (0–5 mM)) and ionic species (i.e., Cl^- (0–10 mM), NO_3^- (0–10 mM), HCO_3^- (0–2 mM), Ca^{2+} (0–2 mM) and Mg^{2+} (0–5 mM)) in real wastewater (Fig. S10). The environmental temperature has little effect on Force/ BFO NSs /PDS system (Fig. S11). More importantly, the system possesses high tolerance to the environmental pH and the removal efficiency of BPA at 30 min is > 95.2% in the initial pH range of 2.5–9.2 (Fig. S12). The Force/BFO NSs/PDS system still can remove 70.5% of BPA in 30 min after 5 cycling experiments, and there is no obvious change in the XRD pattern and morphology of BFO NSs (Fig. S13). After the activation reaction, the dissolved Bi concentration is below the detection limit of the ICP–OES (i.e., 1 mg/L) and the Fe leaching amount shown in Fig. S14 is lower than the environmental standard stipulated by European Union (2 mg/L), thus avoiding the secondary pollution to environment [34]. Furthermore, the removal efficiency of ibuprofen, sulfamethoxazole, carbamazepine, atrazine in the Force/BFO NSs/PDS system exceeds 70% within 30 min (Fig. S15). These results clearly demonstrate the piezocatalytic PDS activation system with BFO NSs holds great potential application in organic wastewater treatment.

To verify the active species generated during piezocatalytic activation of PDS over BFO NSs, a series of quenching experiments were conducted (Fig. S16). With the addition of large amount of MeOH (•OH and $SO_4^{•−}$ quencher, 2000 mM), the degradation efficiency of BPA is only decreased by 13% (Fig. 2c). It is reported that MeOH is hydrophilic compound and preferable to scavenge free radicals in liquid phase compared with surface-bound $SO_4^{•−}$ and •OH [35,36]. Thus, to further explore the generation of catalyst surface-bound $SO_4^{•−}$ and •OH, both PhOH and EtOH (•OH and $SO_4^{•−}$ quencher), which could easily accumulate on the surface of catalyst and react with surface-bound $SO_4^{•−}$ and •OH [8,37–39], were employed for quenching experiments. The addition of PhOH (3 mM) and EtOH (2000 mM) reduce the degradation efficiencies of BPA from 98.3% to 7.5% and 10.2%, respectively (Fig. 2c). Moreover, the BPA degradation efficiency is decreased by 31.4% upon addition of TBA (•OH quencher, 2000 mM) (Fig. 2c). As shown in Fig. 2d, the EDTA (holes quencher, 0.01 mM) inhibits the BPA removal by 12.2%. Meanwhile, the BPA removal is reduced from 98.3% to 76.9% and 79.2% with the addition of the NaN_3 ($^1O_2$ quencher, 1 mM) and FFA ($^1O_2$ quencher, 2 mM), respectively (Figs. 2c and S17). When the p-BQ ($O_2^{•−}$ quencher, 1 mM) is added, the degradation efficiency of BPA is reduced to 72.8% (Fig. 2c), which is very closed to the resulted obtained using $^1O_2$ quencher (NaN_3 and FFA). As the $O_2^{•−}$

possesses limited reaction activity with BPA and can readily to form $^1O_2$ [3,40,41], it is believed the generated $O_2^{•−}$ contributes to the BPA degradation via formation of $^1O_2$. Therefore, both •OH and $SO_4^{•−}$ are the major reactive species contributing to the BPA degradation, and the $^1O_2$ and holes also contribute the BPA removal in piezocatalytic activation of PDS over BFO NSs.

To directly confirm the role of active species, EPR analyses were performed with DMPO and TEMP trapping agents. The characteristic signals of the DMPO-$SO_4^{•−}$, DMPO-•OH and TEMP-$^1O_2$, DMPO- $O_2^{•−}$ adducts are identified (Figs. 2e , f and S18a), implying the generation of $SO_4^{•−}$, •OH, $^1O_2$ and $O_2^{•−}$. Furthermore, the DMPO-$SO_4^{•−}$ and DMPO-•OH peaks almost disappear in the presence of 3 mM PhOH and 2000 mM EtOH, while the peak intensity of TEMP-$^1O_2$ only decrease slightly with the addition of 3 mM PhOH and 2000 mM EtOH, suggesting 3 mM PhOH and 2000 mM EtOH can effectively quench $SO_4^{•−}$ and •OH without quench much $^1O_2$. Combined with the EPR analyses and quenching experiments, it can conclude that the $SO_4^{•−}$ and •OH are the major active species for BPA degradation.

To understand the degradation pathway of BPA, the generated intermediates of BPA degradation was identified via GC-MS. The detected intermediate products are p-isopropenyl phenol ($m/z = 134$), 4-hydroxyacetophenone ($m/z = 135$), phenol ($m/z = 94$) and p-hydroxylphenol ($m/z = 110$). Based on the above results and previous reports [42,43], the possible degradation pathway of BPA in Force/BFO NSs/PDS system was proposed in Fig. S19. Firstly, BPA is attacked by active species to produce p-isopropenyl phenol and phenol. Subsequently, p-isopropenyl phenol is oxidized to p-hydroxylphenol via the intermediate product of 4-hydroxyacetophenone and the phenol also transformed into p-hydroxylphenol by the oxidation of •OH. Finally, the p-hydroxylphenol was further oxidized to generate the ring-opened products and mineralized into CO_2 and H_2O.

3.3. Mechanistic insight

3.3.1. Catalytic mechanism of BFO NSs for PDS activation

To reveal the dynamic catalytic process for PDS activation via BFO NSs with high exposure of {001} facets, the adsorption/activation of PDS on the {001} facets of BFO NSs were explored by ab initio molecular dynamics approach. The $S_2O_8^{2−}$, which was randomly placed on the $Bi_2Fe_4O_9$ crystals at the beginning, was preferentially adsorbed on Fe sites of FeO_4, and then the $S_2O_8^{2−}$ was activated to form $SO_4^{•−}$ via breaking the O–O bond (Fig. 3a and Fig. S20). The energy barrier for the PDS activation was as low as 0.425 eV (Fig. 3b), and the energy of product was lower than that of the reactant, indicating that the PDS activation reaction is thermodynamically favorable, which is consistent with its superior catalytic performance in PDS system.

To explore the electron transfer behaviors during the PDS activation, the spin charge density distribution of the $S_2O_8^{2−}$ and $Bi_2Fe_4O_9$ before and after catalytic process was calculated by DFT approach (Figs. 3c and S21). As can be seen, the spin charge density distribution around Fe atoms in $Bi_2Fe_4O_9$ and O atoms in $S_2O_8^{2−}$ changes before and after activation, suggesting there is electron-transfer during $S_2O_8^{2−}$ activation process. The Bader charge results indicate that the charge on $S_2O_8^{2−}$ before and after activation is − 1.543 and − 2.486 respectively (Figs. 3d and S22), clearly demonstrating Fe^{2+} in $Bi_2Fe_4O_9$ nanocrystals donate ~0.943 electron to $S_2O_8^{2−}$ for $SO_4^{•−}$ generation. Based on the above theoretical calculations, it is clear that the PDS is activated to generate $SO_4^{•−}$ by accepting the electrons from Fe^{2+} in $Bi_2Fe_4O_9$, which accompanied with the breaking of O-O bond in $S_2O_8^{2−}$.

To confirm the understanding based on DFT calculations (i.e., the role of Fe^{3+}/Fe^{2+} redox in PDS activation), the high resolution XPS spectra of Fe 2p in BFO NSs before and after activation PDS were explored. For the fresh BFO NSs, the $Fe2p_{3/2}$ spectrum could be deconvoluted into two peaks at 709.6 eV and 711 eV (Fig. 4a), suggesting the co-existence of Fe^{2+} and Fe^{3+} in catalyst [44,45]. For used BFO NSs in BFO NSs/PDS system, the proportion of Fe^{2+} in BFO NSs
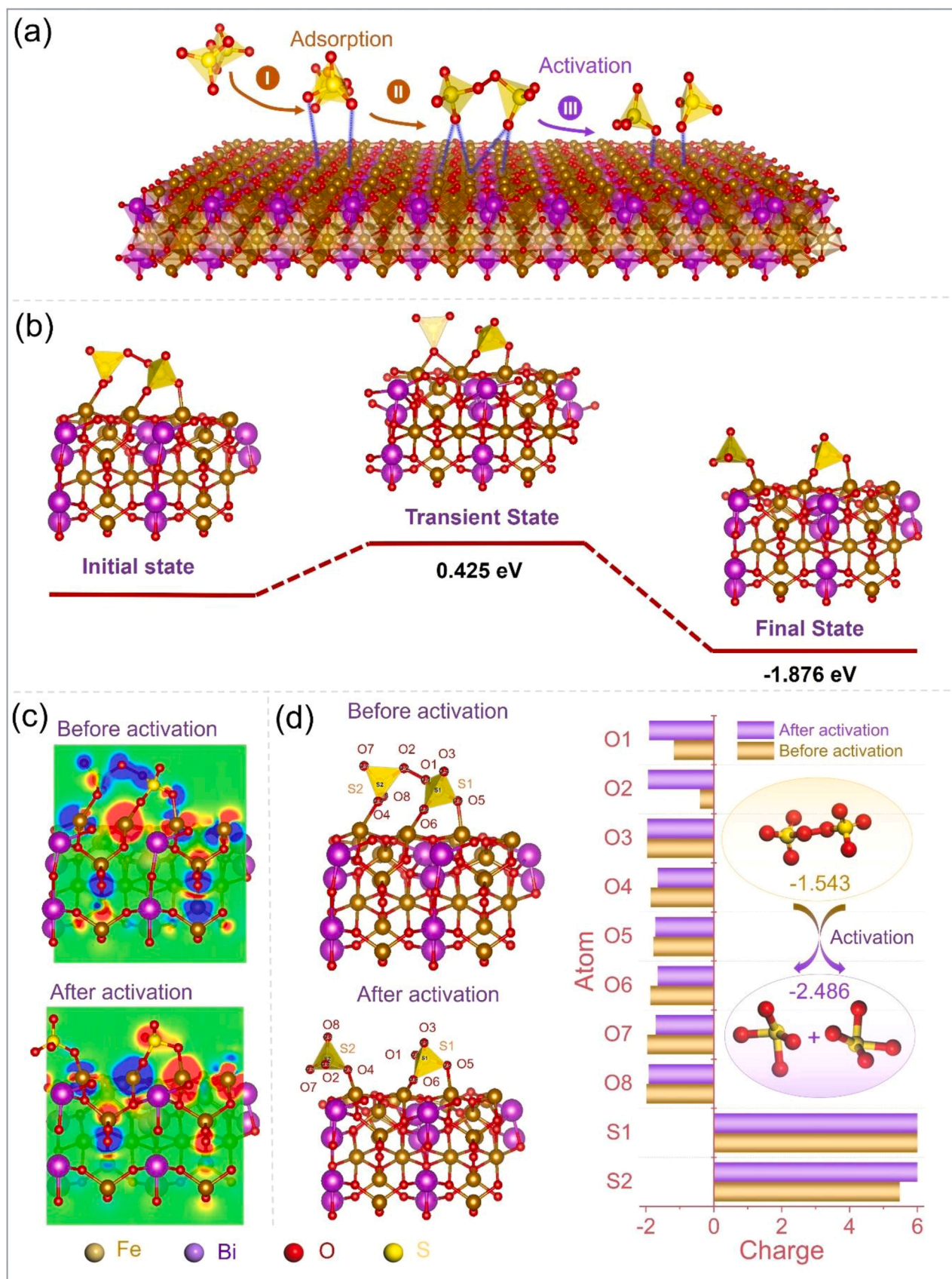
Fig. 3. (a) Adsorption and activation of $S_2O_8^{2-}$ and (b) activation pathway of $S_2O_8^{2-}$ on $Bi_2Fe_4O_9$ crystal. (c) Spin charge density of before and after $S_2O_8^{2-}$ activation. (d) Bader charge for $S_2O_8^{2-}$ before and after activation.
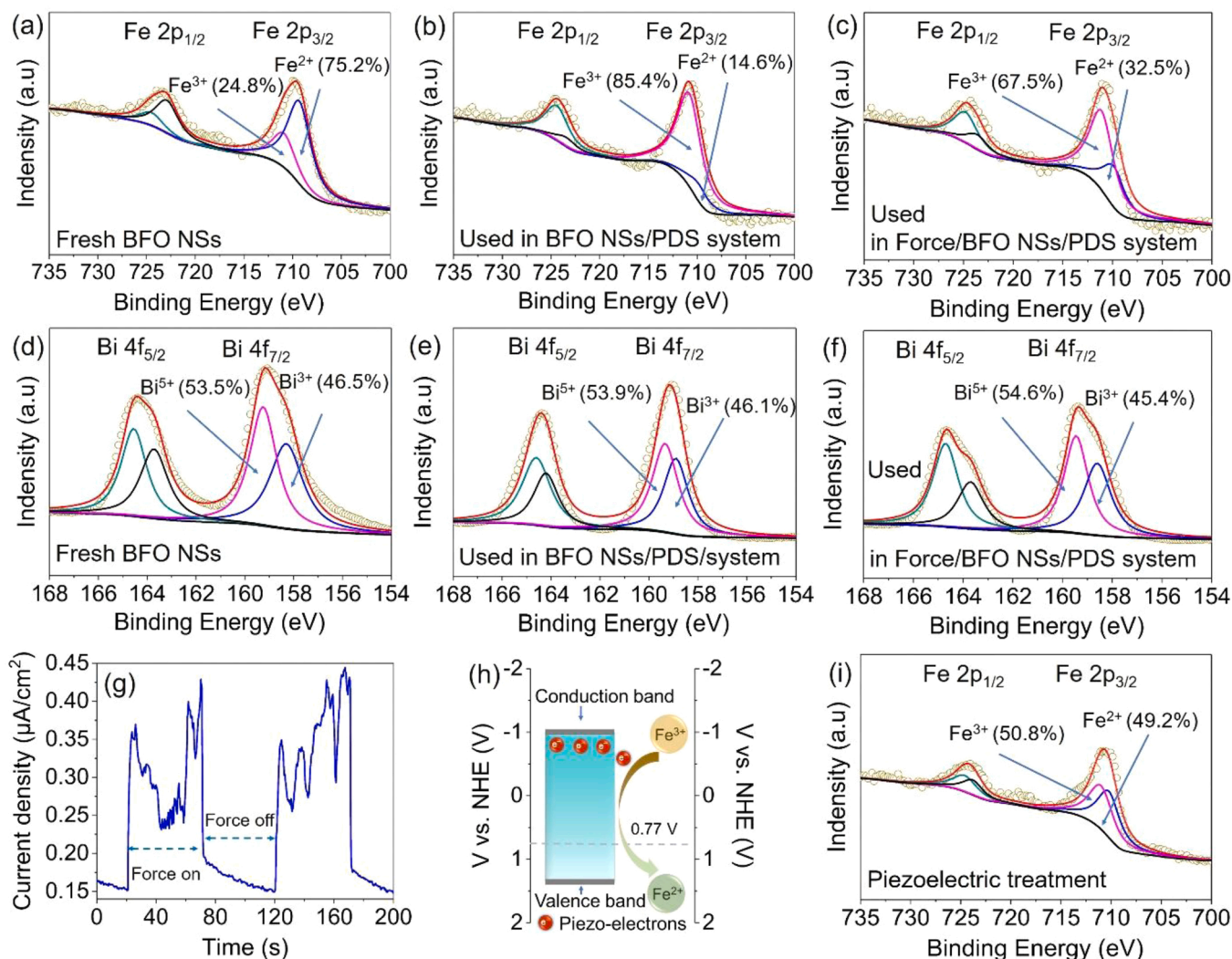
Fig. 4. High resolution XPS spectra of (a, b, c) Fe2p and (d, e, f) Bi 4f before and after activation for BFO NSs. (g) piezo-current density and (h) energy band diagram of BFO NSs. (i) XPS spectra of Fe2p after piezoelectric treatment.

decreases from 75.2% to 14.6% (Fig. 4b), suggesting partial Fe^{2+} in BFO NSs was oxidized to Fe^{3+} during PDS activation process. Furthermore, the Bi 4 $f_{7/2}$ can split into two peaks at 158.6 eV and 159.4 eV (Fig. 4d), corresponding to the Bi^{3+} and Bi^{5+} in the catalyst, respectively [46,47]. After reaction in BFO NSs/PDS and Force/BFO NSs/PDS systems, the change of the content of Bi^{3+} in catalyst is not obvious (Fig. 4e and f), indicating the oxidation of Bi^{3+} is negligible during PDS activation process. These results demonstrate the Fe^{3+}/Fe^{2+} redox is responsible for the electron transfer during the PDS activation, consistent with the understanding from DFT calculations.

3.3.2. Piezo-promoted Fe^{3+}/Fe^{2+} circulation

To explore the role of piezoelectricity on BFO NSs for PDS activation, the piezoelectric current measurement was performed to investigate the influence of piezo-electrons on Fe^{3+}/Fe^{2+} circulation in the BFO NSs. The current output of BFO NSs increases quickly under the applied force (Fig. 4g), suggesting the force-induced piezoelectric field can drive free charges separation [17,48]. Furthermore, the conductive band potential of BFO NSs is calculated to be − 0.88 V vs. NHE (Fig. S24), which is more negative than the reduced potential of Fe^{3+}/Fe^{2+} (0.77 V vs. NHE), implying that the piezo-electrons could reduce Fe^{3+} to Fe^{2+} (Fig. 4h). To confirm the role of piezo-electrons, the Fe 2p spectra of used BFO NSs in BFO NSs/PDS and Force/BFO NSs/PDS systems were investigated (Fig. 4b, c and Fig. S25). The Fe^{2+} proportion in BFO NSs

used in Force/BFO NSs/PDS system (1400 rpm) is higher than that used in BFO NSs/PDS system (32.5% vs. 14.6%), and the proportion of Fe^{2+} of used BFO NSs in Force/BFO NSs/PDS system increases with the increase of applied forces (i.e., 23.9%, 28.5% and 32.5% at the speeds of 500, 1000 and 1400 rpm, respectively). Meanwhile, as shown in Fig. 4i, the Fe^{2+} ratio of BFO NSs used in Force/BFO NSs/PDS system increases from 32.5% to 49.2% after piezoelectric treatment (i.e., BFO NSs aqueous suspension under magnetic stirring). In addition, the bulk phase Fe^{2+} concentrations of BFO NSs used in Force/BFO NSs/PDS and BFO NSs/PDS systems were evaluated by method reported by Xu et al. [49]. As shown in Fig. S26, after the reaction, the bulk phase Fe^{2+} concentration of BFO NSs used in Force/BFO NSs/PDS system is higher than that of BFO NSs/PDS system, which is in accordance with XPS analyses. These results clearly demonstrate that the piezo-electrons can accelerate the reduction of Fe^{3+} to Fe^{2+}, thus enhancing the piezocatalytic PDS activation performance of BFO NSs.

Based on the above results and analyses, a possible mechanism of piezo-catalyzing PDS activation over BFO NSs was proposed in Fig. 5. First, the $S_2O_8^{2-}$ is preferentially absorbed by Fe sites in BFO NSs, and then Fe^{2+} donate electrons for $S_2O_8^{2-}$ activation to generate $SO_4^{•-}$ and •OH (Eqs. 1 and 2). Meanwhile, the $^1O_2$ could be generated (Eqs. 3 and 4) [40,41]. Furthermore, the BFO NSs could deform under the applied force and induce the generation of piezo-electrons and holes (Eq. 5), and the piezo-electrons could facilitate the reduction of Fe^{3+} to form Fe^{2+}
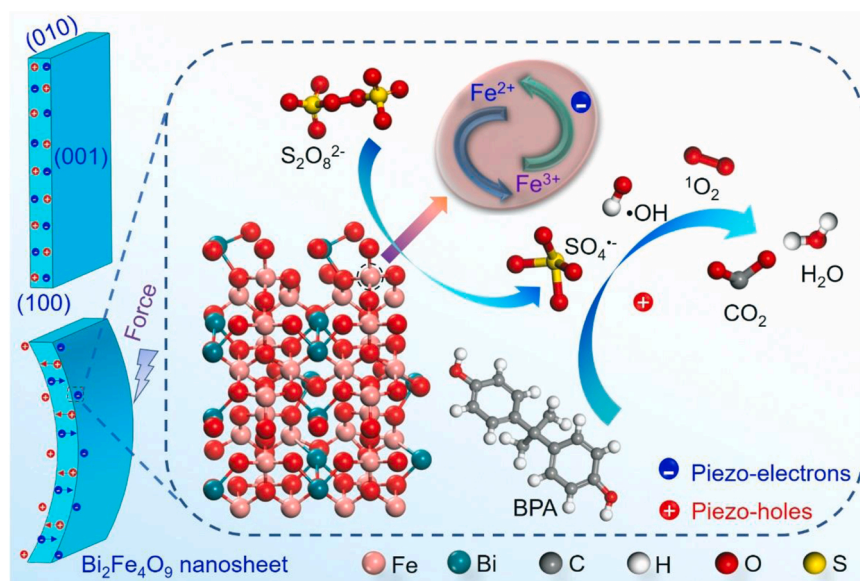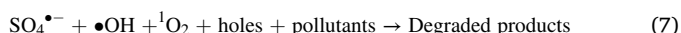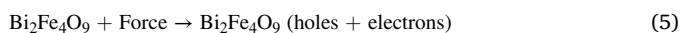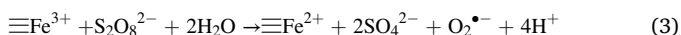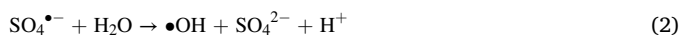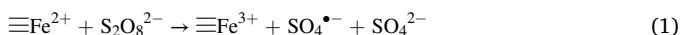
Fig. 5. Proposed mechanism of BFO NSs piezo-catalyzing PDS activation.

active sites (Eq. 6), thus resulting in the remarkable piezocatalytic PDS activation performance. The $SO_4^{\bullet-}$, $\bullet OH$, $^1O_2$ and holes can directly oxidize the organic pollutants (Eq. 7).

$$\equiv Fe^{2+} + S_2O_8^{2-} \rightarrow \equiv Fe^{3+} + SO_4^{\bullet-} + SO_4^{2-} \tag{1}$$

$$SO_4^{\bullet-} + H_2O \rightarrow \bullet OH + SO_4^{2-} + H^+ \tag{2}$$

$$\equiv Fe^{3+} + S_2O_8^{2-} + 2H_2O \rightarrow \equiv Fe^{2+} + 2SO_4^{2-} + O_2^{\bullet-} + 4H^+ \tag{3}$$

$$2O_2^{\bullet-} + 2H_2O \rightarrow H_2O_2 + {}^1O_2 + 2OH^- \tag{4}$$

$$Bi_2Fe_4O_9 + Force \rightarrow Bi_2Fe_4O_9 \text{ (holes + electrons)} \tag{5}$$

$$\equiv Fe^{3+} + electrons \rightarrow \equiv Fe^{2+} \tag{6}$$

$$SO_4^{\bullet-} + \bullet OH + {}^1O_2 + holes + pollutants \rightarrow Degraded products \tag{7}$$

4. Conclusion

In this work, the BFO NSs with piezoelectricity were synthesized to uncover the catalytic sites, mechanism and critical role of piezo-electrons of BFO NSs in piezocatalytic PDS activation. The experimental results demonstrate that the PDS activation performance is remarkably enhanced by the piezoelectricity of BFO NSs. The quenching experiments and EPR analyses confirm that the $SO_4^{\bullet-}$ and $\bullet OH$ are the major active species for organic pollutant degradation. The DFT calculations and XPS analyses indicate that the PDS is activated to generate $SO_4^{\bullet-}$ by accepting the electrons from active centers of Fe^{2+} in the BFO NSs. It is also found the piezoelectricity of BFO NSs facilitates the charge separation and piezo-electrons can accelerate the regeneration of Fe^{2+}, thus resulting in excellent piezocatalytic PDS activation performance. This work provides atomic scale understandings on catalytic mechanisms of piezocatalytic PDS activation over piezocatalyst, serving as guidelines for the further development of piezocatalytic advanced oxidation processes.

CRediT authorship contribution statement

Chuangjian Su: Project designing, Experiments, Data analysis, Writing – original draft, Editing. **Ruhong Li:** Designing and conducting DFT calculations. **Chaolin Li:** Project designing, Editing, Supervision, Funding acquisition. **Wenhui Wang:** Idea conceiving, Project designing,

Writing – original draft, Writing – review & editing, Supervision, Funding acquisition.

Declaration of Competing Interest

The authors declare that they have no known competing financial interests or personal relationships that could have appeared to influence the work reported in this paper.

Acknowledgements

Credit author statement

The authors agree to act as guarantors for the accuracy and legitimacy of the whole paper and in particular any original data presented.

Appendix A. Supporting information

Supplementary data associated with this article can be found in the online version at doi:10.1016/j.apcatb.2022.121330.

References

[1] Y. Chen, G. Zhang, H.J. Liu, J.H. Qu, Confining free radicals in close vicinity to contaminants enables ultrafast fenton-like processes in the interspacing of MoS_2 membranes, Angew. Chem. Int. Ed. 58 (2019) 8134–8138.

[2] B. Hodges, E.L. Cates, K. Jae-Hong, Challenges and prospects of advanced oxidation water treatment processes using catalytic nanomaterials, Nat. Nanotechnol. 13 (2018) 642–650.

[3] X.Q. Zhou, A. Jawad, M.Y. Luo, C.G. Luo, T.T. Zhang, H.B. Wang, J. Wang, S.L. Wang, Z.L. Chen, Z.Q. Chen, Regulating activation pathway of Cu/Persulfate through the incorporation of unreducible metal oxides: pivotal role of surface oxygen vacancies, Appl. Catal., B 286 (2021) 119914.

[4] L.D. Lai, H.D. Ji, H. Zhang, R. Liu, C.Y. Zhou, W. Liu, Z.M. Ao, N.W. Li, C. Liu, G. Yao, B. Lai, Activation of peroxydisulfate by V-Fe concentrate ore for enhanced degradation of carbamazepine: Surface $\equiv V(III)$ and $\equiv V(IV)$ as electron donors promoted the regeneration of $\equiv Fe(II)$, Appl. Catal. B 282 (2021), 119559.

[5] S.Y. Qu, W.H. Wang, X.Y. Pan, C.L. Li, Improving the fenton catalytic performance of FeOCl using an electron mediator, J. Hazard. Mater. 384 (2019), 121494.

[6] Z.Y. Yang, X. Li, Y.Z. Huang, Y.W. Chen, A.Q. Wang, Y.C. Wang, C.H. Li, Z.F. Hu, K. Yan, Facile synthesis of cobalt-iron layered double hydroxides nanosheets for

direct activation of peroxymonosulfate (PMS) during degradation of fluoroquinolones antibiotics, J. Clean. Prod. 310 (2021), 127584.

[7] Y.F. Tong, P. Zhou, Y. Liu, N.R. Wang, W. Li, F. Cheng, B. Yang, J. Liang, Y. L. Zhang, B. Lai, Strongly enhanced fenton-like oxidation (Fe/peroxydisulfate) by BiOI under visible light irradiation: a novel and green strategy for Fe (III) reduction, J. Hazard. Mater. 428 (2022), 128202.

[8] Z.Y. Guo, C.X. Li, M. Gao, X. Han, Y.J. Zhang, W.J. Zhang, W.W. Li, Mn-O covalency governs the intrinsic activity of Co-Mn spinel oxides for boosted peroxymonosulfate activation, Angew. Chem. Int. Ed. 60 (2021) 274–280.

[9] Y.W. Feng, L.L. Ling, Y.X. Wang, Z.M. Xu, F.L. Cao, H.X. Li, Z.F. Bian, Engineering spherical lead zirconate titanate to explore the essence of piezo-catalysis, Nano Energy 40 (2017) 481–486.

[10] W. Wu, L. Wang, Y. Li, F. Zhang, L. Lin, S. Niu, D. Chenet, X. Zhang, Y. Hao, T. F. Heinz, J. Hone, Z.L. Wang, Piezoelectricity of single-atomic-layer MoS2 for energy conversion and piezotronics, Nature 514 (2014) 470–474.

[11] Z. Liang, C.H. Yan, S. Rtimi, J. Bandara, Piezoelectric materials for catalytic/photocatalytic removal of pollutants: recent advances and outlook, Appl. Catal. B 241 (2019) 256–269.

[12] A. Zhang, Z.Y. Liu, B. Xie, J.S. Lu, K. Guo, S.M. Ke, L.L. Shu, H.Q. Fan, Vibration catalysis of eco-friendly Na0.5K0.5NbO3-based piezoelectric: an efficient phase boundary catalyst, Appl. Catal. B 279 (2020), 119353.

[13] J.M. Wu, W.E. Chang, Y.T. Chang, C.K. Chang, Piezo-catalytic effect on the enhancement of the ultra-high degradation activity in the dark by single- and few-layers MoS2 nanoflowers, Adv. Mater. 28 (2016) 3718–3725.

[14] L. Pan, S.C. Sun, Y. Chen, P.H. Wang, J.Y. Wang, X.W. Zhang, J.J. Zou, Z.L. Wang, Advances in piezo-phototronic effect enhanced photocatalysis and photoelectrocatalysis, Adv. Energy Mater. 10 (2020), 2000214.

[15] H.W. Huan, S.C. Tu, C. Zeng, T.R. Zhang, A.H. Reshak, Y.H. Zhang, Macroscopic polarization enhancement promoting photo- and piezoelectric-induced charge separation and molecular oxygen activation, Angew. Chem. Int. Ed. 56 (2017) 11860–11864.

[16] S. Lan, Y. Chen, L. Zeng, H. Ji, M. Zhu, Piezo-activation of peroxymonosulfate for benzothiazole removal in water, J. Hazard. Mater. 393 (2020), 122448.

[17] F. Peng, R. Yin, Y. Liao, X. Xie, J.L. Sun, D.H. Xia, C. He, Kinetics and mechanisms of enhanced degradation of ibuprofen by piezo-catalytic activation of persulfate, Chem. Eng. J. 392 (2020), 123818.

[18] D. Xia, Z. Tang, Y. Wang, R. Yin, G. Zhang, Piezo-catalytic persulfate activation system for water advanced disinfection: process efficiency and inactivation mechanisms, Chem. Eng. J. 400 (2020), 125894.

[19] Y.X. Chen, S.Y. Lan, M.S. Zhu, Construction of piezoelectric BaTiO3/MoS2 heterojunction for boosting piezo-activation of peroxymonosulfate, Chin. Chem. Lett. 32 (2021) 2052–2056.

[20] Y. Gao, T.W. Wu, C.D. Yang, C. Ma, Z.Y. Zhao, Z.H. Wu, S.J. Cao, W. Geng, Y. Wang, Y.Y. Yao, Y.N. Zhang, C. Cheng, Activitytrends and mechanisms in peroxymonosulfate-assisted catalytic production of singlet oxygen over atomic metal-N-C catalysts, Angew. Chem. Int. Ed. 60 (2021) 22513–22521.

[21] J. Li, Y.J. Wan, Y.J. Li, G. Yao, B. Lai, Surface Fe(III)/Fe(II) cycle promoted the degradation of atrazine by peroxymonosulfate activation in the presence of hydroxylamine, Appl. Catal. B 256 (2019), 117782.

[22] H.H. Liu, L. Li, C.F. Guo, J.Q. Ning, Zhong Yi Jun, Y. Hu, Thickness-dependent carrier separation in Bi2Fe4O9 nanoplates with enhanced photocatalytic water oxidation, Chem. Eng. J. 385 (2019), 123929.

[23] H.L. You, Z. Wu, L.H. Zhang, Y.R. Ying, Y. Liu, L.F. Fei, X.X. Chen, Y.M. Jia, Y. J. Wang, F.F. Wang, S. Ju, J.L. Qiao, C.H. Lam, H.T. Huang, Harvesting the vibration energy of BiFeO3 nanosheets for hydrogen evolution, Angew. Chem. Int. Ed. 58 (2019) 11779–11784.

[24] S. Qu, W. Wang, X. Pan, C. Li, Improving the fenton catalytic performance of FeOCl using an electron mediator, J. Hazard. Mater. 384 (2019), 121494.

[25] J. Vandevondele, M. Krack, F. Mohamed, M. Parrinello, T. Chassaing, J. Hutter, QUICKSTEP: fast and accurate density functional calculations using a mixed Gaussian and plane waves approach, Comput. Phys. Commun. 167 (2005) 103–128.

[26] G. Henkelman, B.P. Uberuaga, H. JoNsson, A climbing image nudged elastic band method for finding saddle points and minimum energy paths, J. Chem. Phys. 113 (2000) 9901–9904.

[27] W. Wang, L. Shi, D. Lan, Q. Li, Improving cycle stability of SnS anode for sodium-ion batteries by limiting Sn agglomeration, J. Power Sources 377 (2018) 1–6.

[28] Q. Xiang, J. Yu, W. Wang, M. Jaroniec, Nitrogen self-doped nanosized TiO2 sheets with exposed {001} facets for enhanced visible-light photocatalytic activity, Chem. Commun. 47 (2011) 6906–6908.

[29] C.X. Zhang, D. Lei, C.F. Xie, X.S. Hang, C.X. He, H.L. Jiang, Piezo-photocatalysis over metal-organic frameworks: promoting photocatalytic activity by piezoelectric effect, Adv. Mater. (2021), 2106308.

[30] Y. Wang, X.R. Wen, Y.M. Jia, M. Huang, F.F. Wang, X.H. Zhang, Y.Y. Bai, G. L. Yuan, Y.J. Wang, Piezo-catalysis for nondestructive tooth whitening, Nat. Commun. 11 (2020) 1328.

[31] Y. Chen, X.M. Deng, J.Y. Wen, J. Zhu, Z.F. Bian, Piezo-promoted the generation of reactive oxygen species and the photodegradation of organic pollutants, Appl. Catal. B 258 (2019), 118024.

[32] D.F. Yu, Z.H. Liu, J.M. Zhang, S. Li, Z.C. Zhao, L.F. Zhu, W.S. Liu, Y.H. Lin, H. Liu, Z.T. Zhang, Enhanced catalytic performance by multi-field coupling in KNbO3 nanostructures: Piezo-photocatalytic and ferro-photoelectrochemical effects, Nano Energy 58 (2019) 695–705.

[33] Y.F. Wang, Y.M. Xu, S.S. Dong, P. Wang, W. Chen, Z.D. Lu, D.J. Ye, B.C. Pan, D. Wu, C. Vecitis, G.D. Gao, Ultrasonic activation of inert poly(tetrafluoroethylene) enables piezocatalytic generation of reactive oxygen species, Nat. Commun. 12 (2021) 3508.

[34] J.T. Tang, J.L. Wang, Metal organic framework with coordinatively unsaturated sites as efficient fenton-like catalyst for enhanced degradation of sulfamethazine, Environ. Sci. Technol. 52 (2018) 5367–5377.

[35] L. Hu, G. Zhang, Q. Wang, Y. Sun, M. Liu, P. Wang, Facile synthesis of novel Co3O4-Bi2O3 catalysts and their catalytic activity on bisphenol A by peroxymonosulfate activation, Chem. Eng. J. 326 (2017) 1095–1104.

[36] X. Wang, Y. Qin, L. Zhu, H. Tang, Nitrogen-doped reduced graphene oxide as a bifunctional material for removing bisphenols: synergistic effect between adsorption and catalysis, Environ. Sci. Technol. 49 (2015) 6855–6864.

[37] Y. Feng, P.H. Lee, D. Wu, K. Shih, Surface-bound sulfate radical-dominated degradation of 1,4-dioxane by alumina-supported palladium (Pd/Al2O3) catalyzed peroxymonosulfate, Water Res. 120 (2017) 12–21.

[38] H. Chen, Y. Xu, K. Zhu, H. Zhang, Understanding oxygen-deficient La2CuO4-δ perovskite activated peroxymonosulfate for bisphenol A degradation: the role of localized electron within oxygen vacancy, Appl. Catal. B 284 (2020), 119732.

[39] S. Yan, W. Xiong, S. Xing, Y. Shao, R. Guo, H. Zhang, Oxidation of organic contaminant in a self-driven electro/natural maghemite/peroxydisulfate system: efficiency and mechanism, Sci. Total Environ. 599–600 (2017) 1181–1190.

[40] S.S. Zhu, X.J. Li, J. Kang, X.G. Duan, S.B. Wang, Persulfate activation on crystallographic manganese oxides: mechanism of singlet oxygen evolution for nonradical selective degradation of aqueous contaminants, Environ. Sci. Technol. 53 (2018) 307–315.

[41] W. Yang, X. Li, Z. Jiang, C. Li, Q. Liao, Structure-dependent catalysis of Co3O4 crystals in persulfate activation via nonradical pathway, Appl. Surf. Sci. 525 (2020), 146482.

[42] M.M. Wang, Y.K. Cui, H.Y. Cao, P. Wei, C. Chen, X.Y. li, J. Xu, G.P. Sheng, Activating peroxydisulfate with Co3O4/NiCo2O4 double-shelled nanocages to selectively degrade bisphenol A – a nonradical oxidation process, Appl. Catal. B 282 (2021), 119585.

[43] Z.Y. Dong, Q. Zhang, B.Y. Chen, J.M. Hong, Oxidation of bisphenol A by persulfate via Fe3O4-α-MnO2 nanoflower-like catalyst: mechanism and efficiency, Chem. Eng. J. 357 (2019) 337–347.

[44] C.Q. Tan, X.C. Jian, Y.J. Dong, X. Lu, X.Y. Liu, H.M. Xiang, X.X. Cui, J. Deng, H. Y. Gao, Activation of peroxymonosulfate by a novel EGCE@Fe3O4 nanocomposite: free radical reactions and implication for the degradation of sulfadiazine, Chem. Eng. J. 359 (2019) 594–603.

[45] C.Q. Tan, N.Y. Gao, D.F. Fu, J. Deng, L. Deng, Efficient degradation of paracetamol with nanoscaled magnetic CoFe2O4 and MnFe2O4 as a heterogeneous catalyst of peroxymonosulfate, Sep. Purif. Technol. 175 (2017) 47–57.

[46] K. Wang, Y. Li, G.K. Zhang, J. Li, X.Y. Wu, 0D Bi nanodots/2D Bi3NbO7 nanosheets heterojunctions for efficient visible light photocatalytic degradation of antibiotics: Enhanced molecular oxygen activation and mechanism insight, Appl. Catal. B 240 (2019) 39–49.

[47] H.X. Zhang, Y.Y. Song, L.C. Nengzi, J.F. Gou, B. Li, X.W. Cheng, Activation of persulfate by a novel magnetic CuFe2O4/Bi2O3 composite for lomefloxacin degradation, Chem. Eng. J. 379 (2019), 122362.

[48] X. Wang, J. Song, L. Jin, Z.L. Wang, Direct-current nanogenerator driven by ultrasonic waves, Science 316 (2007) 102–105.

[49] T.Y. Xu, R.L. Zhu, G.Q. Zhu, J.X. Zhu, X.L. Liang, Y.P. Zhu, H.P. He, Mechanisms for the enhanced photo-Fenton activity of ferrihydrite modified with BiVO4 at neutral pH, Appl. Catal. B 212 (2017) 50–58.